Linear PWM Techniques of Asymmetrical Six-Phase Machine With Optimal Current Ripple Performance

Sayan Paul and Kaushik Basu, *Senior Member, IEEE*

***Abstract*—Linear modulation techniques (LMTs) of an asymmetrical six-phase machine (ASPM) with two isolated neutral points synthesize the desired voltage vectors by applying at least five switching states. Different choices of applied voltage vectors, sequences in which they are used, distribution of dwell-times among the redundant switching states give rise to a large number of possible LMTs. It is desirable that these LMTs avoid more than two transitions of a particular inverter leg within a carrier period. Only a subset of existing LMTs of ASPM follows this rule. Through an innovative approach, this article finds a way to account for all possible infinitely many LMTs that follow the rule of at most two transitions per leg. Another important criterion for the selection of an LMT is its current-ripple performance. Therefore, through numerical optimization, this article finds optimal LMTs among the above infinite possible LMTs for all reference voltage vectors in the linear range and for the whole feasible range of a machine parameter. This parameter is related to the leakage inductance of the machine and impacts the current ripple performance of ASPM. An optimal hybrid strategy is proposed with these optimal techniques, which outperforms all existing techniques in terms of the current ripple. The theoretical analysis is validated through simulation in MATLAB and experiments performed up to 3.5 kW on a hardware prototype.**

***Index Terms*—Asymmetrical six-phase induction motor, current-ripple, linear pulsewidth modulation (PWM) technique, multiphase machines, PWM, six-phase drives.**

I. Introduction

MULTIPHASE machines are popular in high-power drives, electric vehicles and railway traction, safety-critical electric aircraft, ship-propulsion, etc., due to having advantages of reduced power rating of per-phase power-electronic drive unit, better fault-tolerance, lesser susceptibility toward space and supply harmonics [1], [2]. Asymmetrical six-phase machine (ASPM), one of the most common multiphase machines, has two sets of balanced three-phase (3ϕ) windings with spatial angular difference of 30° electrical, as shown in Fig. 1. This machine is also known as dual three-phase machine [3], [4], or split-phase machine [5], in the literature.

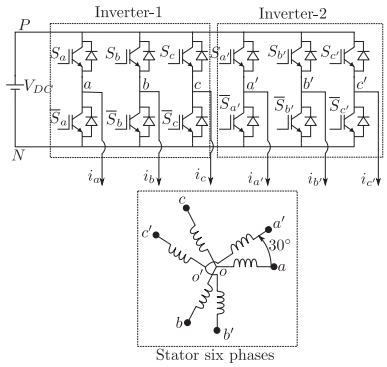

Fig. 1. Six-phase inverter fed ASPM.

Vector-space decomposition based modeling of ASPM, as proposed by [3], transforms the variables from original domain to three 2-D orthogonal subspaces, namely, $\alpha-\beta$, z_1-z_2, and o_1-o_2. It is shown that electromagnetic energy transfer occurs only in $\alpha-\beta$ plane, whereas the remaining two planes do not have coupling between the stator and rotor and hence, are not associated with energy transfer. But, the impedances offered by these two planes are small, so very small excitation in these planes can cause large current and associated copper loss. For two balanced sets of windings with two isolated neutrals, as shown in Fig. 1, o_1-o_2 plane can not be excited. Linear modulation techniques (LMTs) of ASPM synthesize the desired average voltages in $\alpha-\beta$ plane and zero average voltage in z_1-z_2 to avoid the unwanted copper loss. If modulation index (M_I) is defined as the ratio of peak of fundamental line-neutral voltage and dc-bus voltage, the maximum index attainable by LMTs is 0.577. This article focusses on these LMTs and their high-frequency current-ripple performances.

The proposed space-vector based pulsewidth modulation (SVPWM) technique in [3] shows that LMTs of ASPM need to apply at least five distinct vectors. One such set of five

Manuscript received 25 May 2021; revised 18 November 2021 and 14 February 2022; accepted 21 February 2022. Date of publication 9 March 2022; date of current version 5 October 2022. This work was supported by the Ministry of Electronics and Information Technology, Government of India, under the project titled "Design and Development of WBG Device based High Current Converters for Industry Applications." *(Corresponding author: Sayan Paul.)*

The authors are with the Department of Electrical Engineering, Indian Institute of Science, Bangalore 560012, India (e-mail: sayanp@iisc.ac.in; kbasu@iisc.ac.in).

Color versions of one or more figures in this article are available at https://doi.org/10.1109/TIE.2022.3156161.

Digital Object Identifier 10.1109/TIE.2022.3156161

vectors, adopted by [3] and [4], is fourth largest active vectors in $\alpha - \beta$ plane, adjacent to the reference voltage vector, $\vec{V}_{\text{ref}}$, and one zero vector. By placing multiple redundant switching states, corresponding to the zero-vector, at different positions in the switching sequences, Hadiouche *et al.* [4] proposed continuous and discontinuous linear SVPWM techniques with different current-ripple performances, C 6ϕ SVPWM12, D 6ϕ SVPWM12-A/B1/B2. Hadiouche *et al.* [4] showed that the current ripple of ASPM is not only function of PWM techniques, but it also depends upon machine parameter, γ, which is defined as the ratio of high-frequency inductances seen by $\alpha - \beta$ and $z_1 - z_2$ subspaces. To discuss the disadvantages of the proposed SVPWM12 techniques of [4], two desirable features of a PWM technique, as given by *R1* and *R2* in the following paragraph, will be discussed first.

R1. Each semiconductor device of the six-phase inverter is allowed to turn-ON and tun-OFFmaximum one time over a carrier cycle.

R2. The switching sequence will be mirror symmetric along carrier half-period.

Noncompliance of *R1* results in increase in instantaneous switching frequency of a particular leg for the same average switching frequency [6], [7]. Carrier based simple implementation is possible if PWM techniques follow rules *R1* and *R2* [7]. Note, most of the well-known PWM techniques of two-level three-phase inverter, such as SPWM, SVPWM, THIPWMs, and DPWMs, follow these rules for carrier-based implementation [8]. None of the PWM techniques, proposed by [4], follows *R1*. Marouani *et al.* [6] proposed 24 sector based continuous and discontinuous PWM techniques, C 6ϕ SVPWM24, D 6ϕ SVPWM24-B1/B2, where the furthest of the four largest vectors in $\alpha - \beta$ is replaced by one small vector. These techniques follow both the rules. The ripple current performance of D 6ϕ SVPWM24-B2 (the best technique in [6]) is worse than that of D 6ϕ SVPWM12-B1/B2 techniques for the same average switching frequency at higher M_I and higher values of γ. A modified SVPWM24 technique, C 6ϕ SVPWM24-C, is proposed in [7], which also obeys *R1* and *R2* but current-ripple performance is not good at higher M_I and higher values of γ.

Another group of LMTs were proposed by [9] and [10], where two 3ϕ inverters, Inverter-1 and Inverter-2 of Fig. 1, are modulated with the reference voltage vectors $\frac{\vec{V}_{\text{ref}}}{2}$ and $\frac{\vec{V}_{\text{ref}}}{2}e^{-j30^\circ}$, respectively. Paul and Basu [11] showed that this operation is equivalent to synthesizing $\vec{V}_{\text{ref}}$ in $\alpha - \beta$ and zero in $z_1 - z_2$ on average. These techniques are termed as two-inverter based technique (TINV) in [11]. Existing TINV techniques are 1) Sine-triangle PWM (STPWM) [5], where zero common-mode voltage is injected between load-neutral and dc-bus mid-point; 2) Double zero-sequence injection PWM (DZIPWM), which is also named as ZS3PWM in [5], where two different zero-sequence signals are used for two 3ϕ inverters and the modulation signals of both inverters are compared with same carrier signal; these zero-sequence signals are half of the middle values of the corresponding 3ϕ modulation signals; 3) ZS6PWM [5], where a single common-mode signal is used for both Inverter-1 and Inverter-2 and this is equal to the half of negative summation of maximum and minimum of 6ϕ modulating waves. These three TINV techniques follow rules *R1* and *R2*. The comparison of current ripple performances as function of M_I of these TINV techniques and SVPWM techniques reveals that SVPWM techniques are much better than TINV techniques for the feasible range of γ [5], [12].

TABLE I
SWITCHING STATES OF THREE-PHASE INVERTER

S_a	S_b	S_c	Label	S_a	S_b	S_c	Label
Off	Off	Off	0	Off	On	On	4
On	Off	Off	1	Off	Off	On	5
On	On	Off	2	On	Off	On	6
Off	On	Off	3	On	On	On	7

Note, existing three TINV techniques, three techniques proposed in [6], and C 6ϕ SVPWM24-C satisfy the desirable two rules, *R1* and *R2*. In fact, there are infinitely many PWM techniques, not just these seven techniques known in the literature, which satisfy these desirable conditions. This infinite possibility arises due to infinite number of choices of distributions of the dwell-times between two redundant zero states of both 3ϕ inverters, Inverter-1 and Inverter-2 of Fig. 1, in the sequence. It is known from the two-level 3ϕ inverter literature that this distribution impacts the current ripple [8], [13], [14]. In this context, this article makes following contributions.

1) First attempts to identify the complete set of possible LMTs, which satisfy rules *R1* and *R2*, in Section II.
2) Then through systematic analysis in Section III, it finds the optimal technique that results into minimum current ripple for a given $\vec{V}_{\text{ref}}$ in $\alpha - \beta$, machine parameter, γ, and given average switching frequency.
3) In Section III, it finds all such optimal techniques for all possible $\vec{V}_{\text{ref}}$ in linear range for feasible range of γ.
4) Finally, it proposes a hybrid LMT in Section IV using the optimal techniques obtained in previous step. This LMT outperforms all existing LMTs, which follow *R1* and *R2*, in terms of line current THD.

The superiority of the proposed hybrid technique is validated through experiments and simulations in Section V. Finally, Section VI concludes this article.

II. PROPOSED TWO-INVERTER BASED LMTS

Fig. 1 shows a two-level six-phase (6ϕ) inverter, which can be seen as two three-phase (3ϕ) inverters, Inverter-1 and Inverter-2, respectively, connected across the same dc-bus. The pole points of these two 3ϕ inverters, a, b, c, and a', b', c' are directly connected to the terminals of two sets of 3ϕ windings of an ASPM. These two sets of windings are spatially shifted by 30° electrical and are connected in star with two isolated neutral points o and o'. This 6ϕ inverter has 64 switching states. An ordered pair denotes these states, (p, q'), where p and q denote the switching states of Inverter-1 and Inverter-2, respectively, according to the standard 3ϕ inverter notation as given in Table I.

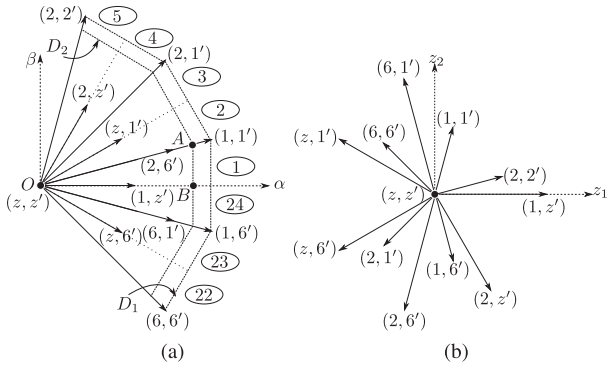

Fig. 2. Mapping of 19 states adjacent to sector-1. (a) $\alpha-\beta$ plane. (b) z_1-z_2 plane.

$$X_i \triangleq \underbrace{\frac{1}{\sqrt{3}}\begin{bmatrix} 1 & -\frac{1}{2} & -\frac{1}{2} & \frac{\sqrt{3}}{2} & -\frac{\sqrt{3}}{2} & 0 \\ 0 & \frac{\sqrt{3}}{2} & -\frac{\sqrt{3}}{2} & \frac{1}{2} & \frac{1}{2} & -1 \\ 1 & -\frac{1}{2} & -\frac{1}{2} & -\frac{\sqrt{3}}{2} & \frac{\sqrt{3}}{2} & 0 \\ 0 & -\frac{\sqrt{3}}{2} & \frac{\sqrt{3}}{2} & \frac{1}{2} & \frac{1}{2} & -1 \\ 1 & 1 & 1 & 0 & 0 & 0 \\ 0 & 0 & 0 & 1 & 1 & 1 \end{bmatrix}}_{T} X_j$$

$$X_i = \begin{bmatrix} x_\alpha & x_\beta & x_{z_1} & x_{z_2} & x_{o_1} & x_{o_2} \end{bmatrix}^T$$

$$X_j = \begin{bmatrix} x_a & x_b & x_c & x_{a'} & x_{b'} & x_{c'} \end{bmatrix}^T \quad . \qquad (1)$$

The matrix, T, as given in (1), was proposed by [3] to model ASPM in three 2-D orthogonal subspaces, namely, $\alpha-\beta$, z_1-z_2, and o_1-o_2. This matrix T is used to map the line-neutral voltages generated by 64 states of 6ϕ inverter into the above six orthogonal planes. It is seen that all 64 states generate zero voltages in o_1-o_2 plane and therefore, discussion in o_1-o_2 plane is excluded in the subsequent sections. The voltage vectors generated by 64 switching states in $\alpha-\beta$ and z_1-z_2 subspaces can be referred from [3] and [5]. These 64 states generate 24 equivalent sectors in $\alpha-\beta$ [6]. The modulation in one of these 24 sectors in $\alpha-\beta$, which is conventionally called as sector-1 [as shown in Fig. 2(a)], can be discussed with the help of 19 switching states. Fig. 2 shows the mapping of these 19 switching states in $\alpha-\beta$ and z_1-z_2 planes and they result into 12 distinct vectors in both the subspaces. In Fig. 2, z denotes zero-state and $z\in\{0,7\}$. Sector numbers in Fig. 2(a) are surrounded by oval-shaped curves. Modulation in the remaining sectors will be similar to sector-1.

LMTs of ASPM synthesize 1) the desired reference voltage vector, $\vec{V}_{\text{ref}} \triangleq \overline{v}_\alpha + j\overline{v}_\beta$, in $\alpha-\beta$ plane as it is solely responsible for electromagnetic energy transfer; 2) zero average voltage vector in nonenergy transferring z_1-z_2 plane in order to avoid unwanted average current and associated copper loss resulted due to the low impedance in this plane, i.e., $\overline{v}_{z_1}+j\overline{v}_{z_2}=0$. Here, bar represents average over a carrier cycle. To generalize the analysis, all lengths in subsequent figures are normalized with respect to dc-bus voltage V_{DC}, and the reference voltage vector is also normalized and denoted by $\vec{m}$. Here, $\vec{m} \triangleq m_\alpha + jm_\beta$ and $m_{\alpha,\beta} = \frac{\overline{v}_{\alpha,\beta}}{V_{\text{DC}}}$. In general, the synthesizable $\vec{m}$ can lie anywhere within a do-decagon structure obtained by joining the tips of the largest vectors in $\alpha-\beta$ plane and D_1 of Fig. 2(a) shows part of this do-decagon. But, Paul and Basu [11] showed that synthesizable $\vec{m}$ of LMTs of ASPM can lie within another smaller do-decagon structure, D_2, due to the constraint of zero average vector synthesis in z_1-z_2. The linear modulation region within sector-1, ΔOAB, is separately shown in Fig. 3, which is a right angle triangle with base length of unity and height of $\tan 15^\circ$.

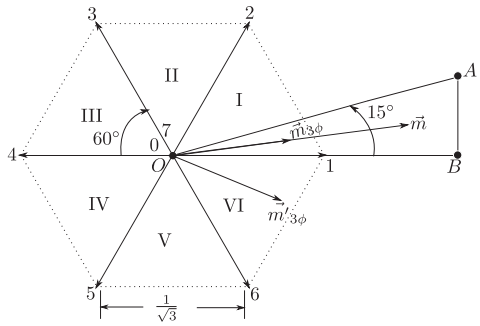

Fig. 3. $\vec{m}$ within ΔOAB and the corresponding $\vec{m}_{3\phi}$ and $\vec{m}'_{3\phi}$.

Paul and Basu [11] showed that synthesis of $\vec{m}$ in $\alpha-\beta$ and zero in z_1-z_2 is mathematically equivalent to modulating the two 3ϕ inverters with reference voltage vectors as follows:

$$\vec{m}_{3\phi} = \frac{1}{2}\vec{m}; \qquad \vec{m}'_{3\phi} = \frac{1}{2}\vec{m}e^{-j30^\circ} \qquad (2)$$

where $\vec{m}_{3\phi}$ and $\vec{m}'_{3\phi}$ are the reference voltage vectors of Inverter-1 and Inverter-2, respectively. These 3ϕ voltage vectors are obtained by applying Clarke's $3\phi-2\phi$ transformation on 3ϕ average line-neutral voltages, as follows:

$$\vec{x}_{3\phi} = \frac{1}{\sqrt{3}}\left[\left(x_a - \frac{x_b}{2} - \frac{x_c}{2}\right) + j\frac{\sqrt{3}}{2}(x_b - x_c)\right]. \qquad (3)$$

With respect to this transformation, the mapping of the line-neutral voltages generated by eight switching states (given in Table I) of 3ϕ inverter is shown in Fig. 3.

Finding all possible LMTs when $\vec{m}\in\Delta OAB$ is equivalent to finding all possible ways to synthesize $\vec{m}_{3\phi}$ and $\vec{m}'_{3\phi}$ in per 3ϕ inverter basis. The intermediate steps, which are followed to derive these techniques from the given $\vec{m}$ in sector-1, are discussed as follows.

A. Determine Vector-Sets Per 3ϕ Inverter and Their Corresponding Duty-Ratios

When $\vec{m}\in\Delta OAB$, $0^\circ \le \angle\vec{m} \le 15^\circ$. Therefore, according to (2), $0^\circ \le \angle\vec{m}_{3\phi} \le 15^\circ$ and $-30^\circ \le \angle\vec{m}'_{3\phi} \le -15^\circ$. Hence, $\vec{m}_{3\phi}$ and $\vec{m}'_{3\phi}$ lie within sector-I and sector-VI, respectively, in complex plane of 3ϕ inverter, as shown in Fig. 3. It is known from the modulation techniques of the conventional 3ϕ inverter that atleast three distinct vectors need to be applied per inverter basis in order to generate these reference voltage vectors. Two

TABLE II
DUTY RATIOS OF THE SWITCHING STATES OF FOUR VECTOR-SETS

Vector-set $\{z,1,2\}$	
$d1$	$\frac{\sqrt{3}}{2}m_\alpha - \frac{1}{2}m_\beta$
$d2$	m_β
dz	$1 - \frac{\sqrt{3}}{2}m_\alpha - \frac{1}{2}m_\beta$

Vector-set $\{6,1,2\}$	
$d1$	$\sqrt{3}m_\alpha - 1$
$d2$	$1 - \frac{\sqrt{3}}{2}m_\alpha + \frac{1}{2}m_\beta$
$d6$	$1 - \frac{\sqrt{3}}{2}m_\alpha - \frac{1}{2}m_\beta$

Vector-set $\{z',1',6'\}$	
$d1'$	$\frac{1}{2}m_\alpha + \frac{\sqrt{3}}{2}m_\beta$
$d6'$	$\frac{1}{2}m_\alpha - \frac{\sqrt{3}}{2}m_\beta$
dz'	$1 - m_\alpha$

Vector-set $\{6',1',2'\}$	
$d1'$	$\frac{3}{2}m_\alpha + \frac{\sqrt{3}}{2}m_\beta - 1$
$d2'$	$1 - m_\alpha$
$d6'$	$1 - \frac{1}{2}m_\alpha - \frac{\sqrt{3}}{2}m_\beta$

very popular choices are 1) nearest two active vectors and one zero vector, 2) nearest three active vectors. Therefore, Inverter-1 can use vector-set $\{z,1,2\}$ or $\{6,1,2\}$ in order to synthesize $\vec{m}_{3\phi}$, where $z \in \{0,7\}$. Similarly, Inverter-2 can use vector-set $\{z,'1,'6'\}$ or $\{6,'1,'2'\}$ to synthesize $\vec{m'}_{3\phi}$. The switching states of Inverter-2 are labeled by primes.

The duty-ratios of each of the vectors of these vector-sets can be found by solving the average voltage equations. For example, d_z, d_1, and d_2, duty-ratios of the vectors of vector-set $\{z,1,2\}$, can be found by solving the following:

$$d_1\frac{1}{\sqrt{3}} + d_2\frac{1}{\sqrt{3}}e^{j60^\circ} = \vec{m}_{3\phi} \triangleq \frac{1}{2}(m_\alpha + jm_\beta); \quad d_1 + d_2 + d_z = 1. \tag{4}$$

d_z, d_1, and d_2 are functions of m_α and m_β. Similarly, duty-ratios of the vectors of other vector-sets can be found. The expressions of these duty-ratios of the above four vector-sets are given in Table II. Note, $\{6,1,2\}$ and $\{6,'1,'2'\}$ can not be used for the entire ΔOAB as $d1$ of $\{6,1,2\}$ and $d1'$ of $\{6,'1,'2'\}$ become negative for some part of ΔOAB. The regions, where $\{6,1,2\}$ and $\{6,'1,'2'\}$ can be used, are identified by solving the inequalities that all the duty-ratios are greater than equal to zero and the respective equations are given as follows:

$$m_\alpha \geq \frac{1}{\sqrt{3}}, \tag{5a}$$

$$\sqrt{3}m_\alpha + m_\beta \geq \frac{2}{\sqrt{3}}. \tag{5b}$$

B. Determine the Sequences of 3ϕ Inverters Corresponding to Each Vector-Set

The sequence design will be guided by rules *R1* and *R2*, as given in Section I. *R2* ensures that all the vectors within the given vector-set need to be applied atleast once within carrier half-period, $\frac{T_s}{2}$. It can be shown that all possible switching sequences of vector-set $\{z,1,2\}$, which obey the above two rules, can be generalized as $0-1-2-7-2-1-0$ within T_s or $0-1-2-7$ within $\frac{T_s}{2}$. From now onward, we will only consider the vector-sequence within $\frac{T_s}{2}$ as the other half is mirror symmetric. Similarly, vector-set $\{z,'1,'6'\}$, $\{6,1,2\}$, and $\{6,'1,'2'\}$ can be generalized as $0'-1'-6'-7'$, $6-1-2$, and $6'-1'-2'$, respectively.

C. Sequence Grouping of 6ϕ Inverter

As each of Inverter-1 and Inverter-2 has two sequences to synthesize $\vec{m}_{3\phi}$ and $\vec{m'}_{3\phi}$, respectively, $\vec{m}$ in $\alpha-\beta$ can be synthesized by using $2\times 2 = 4$ different combinations of 3ϕ sequences. For each of these four combinations, reversal of one sequence to the other gives two different arrangements. Therefore, a total of eight sequence groups can occur, and Table III shows these eight groups. These are labeled as S1–S8. As sequences $0-1-2-7$ and $0'-1'-6'-7'$ can be used to synthesize $\vec{m}$ within the entire ΔOAB, S1 and S2 can be applied for the entire ΔOAB. Similarly, from our previous discussion, it is obvious that S3 and S4 are applicable in the region within ΔOAB, where condition (5b) is satisfied; S5 and S6 are applicable, where (5a) is satisfied, and S7 and S8 are applicable, where both (5a) and (5b) are satisfied. From 3ϕ inverter literature, it is known that the current-ripple is a function of zero-vector splitting [8], [13], [14]. Therefore, the zero-vector dwell-times are split as x, $(1-x)$ (for Inverter-1) and y, $(1-y)$ (for Inverter-2) between redundant zero states 0 and 7 to study the ripple performances in next section. Here, x and y are nonnegative fractions. Note, $x,y \in \{0,1\}$ results into conventional bus-clamping PWM of 3ϕ inverter.

Let us define k_f as the ratio of the total number of switching (combining turn-ON and turn-OFF) over T_s and the total number of legs (6 in this case). As each change of state is accompanied by one transition, $k_f = \frac{m+n-2}{6}$ when the two 3ϕ inverters apply m and n number of states, respectively, within $T_s/2$. From this discussion, one can see that k_f is function of x and y and this function is shown in Table III. As we will see later that k_f plays an important role in current-ripple comparison of different techniques with the same average switching frequency.

D. Determine the Vector Sequence and Corresponding Duty Ratios of 6ϕ Inverter

The objective of this article is to find the best technique in terms of current-ripple out of the infinite number of possible techniques, grouped as S1–S8, for $\vec{m} \in \Delta OAB$. This infinite possibility arises due to the variability in the choice of x and y (S1–S6). Hadiouche *et al.* [4] showed that the estimation of current-ripple requires the sequence of application of 6ϕ switching states (to know the corresponding voltage vectors in both $\alpha-\beta$ and z_1-z_2 planes) and their corresponding dwell times. Given any selection, S1–S8, this sequence and the dwell times of the states depend upon the position of $\vec{m}$, choices of x and y (in case of S1–S6).

To explain the above, let us consider case S7 over $T_s/2$. As S7 involves vector-sets $\{6,1,2\}$ and $\{6,'1,'2'\}$, it can be applied in part of ΔOAB, where both (5a) and (5b) are satisfied. The straight lines with equality in (5a) and (5b) are plotted as CD and ED in Fig. 4. Double-arrow marks on these lines show the part of ΔOAB, where conditions (5a) and (5b) are satisfied and therefore, $\square EDAB$ is the region where S7 can

TABLE III
EIGHT POSSIBLE SEQUENCE-GROUPS WHEN $\vec{m} \in \Delta OAB$

Case	Sequence over $\frac{T_s}{2}$	k_f	Case	Sequence over $\frac{T_s}{2}$	k_f
S1	$\underbrace{0}_{x}\ -1-2-\underbrace{7}_{1-x}$ $\underbrace{0'}_{y}\ -1'-6'-\underbrace{7'}_{1-y}$	$k_f = \begin{cases} 1; x, y \in (0,1) \\ \frac{2}{3}; x, y \in \{0,1\} \\ \frac{5}{6}; \text{O.W.} \end{cases}$	S5	$6-1-2$ $\underbrace{0'}_{y}\ -1'-6'-\underbrace{7'}_{1-y}$	$k_f = \begin{cases} \frac{5}{6}; 0 < y < 1 \\ \frac{2}{3}; y \in \{0,1\} \end{cases}$
S2	$\underbrace{0}_{x}\ -1-2-\underbrace{7}_{1-x}$ $\underbrace{7'}_{y}\ -6'-1'-\underbrace{0'}_{1-y}$		S6	$6-1-2$ $\underbrace{7'}_{y}\ -6'-1'-\underbrace{0'}_{1-y}$	
S3	$\underbrace{0}_{x}\ -1-2-\underbrace{7}_{1-x}$ $6'-1'-2'$	$k_f = \begin{cases} \frac{5}{6}; 0 < x < 1 \\ \frac{2}{3}; x \in \{0,1\} \end{cases}$	S7	$6-1-2$ $6'-1'-2'$	$k_f = \frac{2}{3}$
S4	$\underbrace{0}_{x}\ -1-2-\underbrace{7}_{1-x}$ $2'-1'-6'$		S8	$6-1-2$ $2'-1'-6'$	

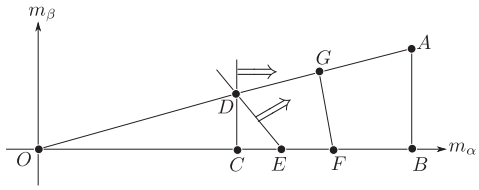

Fig. 4. S7 applied within ΔOAB.

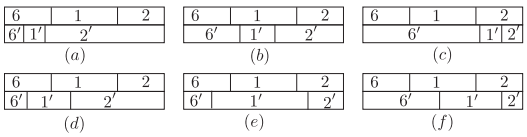

Fig. 5. Six possible arrangements of sequence-group S7.

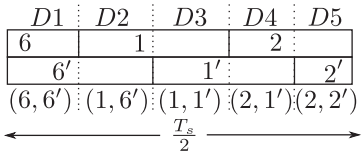

Fig. 6. Sequence of Fig. 5(f).

be applied. Fig. 5 shows all six probable cases of S7, where states of Inverter-1 and Inverter-2 are placed in top and bottom, respectively. From Fig. 5, 6ϕ sequences and the dwell time of each switching state corresponding to a sequence can be determined. For example, sequence of case (*f*) of Fig. 5 is $(6,6') - (1,6') - (1,1') - (2,1') - (2,2')$, as shown in Fig. 6. The corresponding duty-ratios of these states with respect to $T_s/2$ are $D1 = d6$, $D2 = d6' - d6$, $D3 = d1 - (d6' - d6)$, $D4 = d2 - d2'$, and $D5 = d2'$, respectively, where the duty values, dk and dk', $k = 1, 2, 6$, correspond to vector-sets $\{6, 1, 2\}$ and $\{6,' 1,' 2'\}$, respectively, of Table II. Similarly, one can find the sequences for other cases of S7, which are tabulated in Table IV. For a given $\vec{m} \triangleq m_\alpha + jm_\beta$, one of these six cases can occur as the duty ratios are defined by m_α and m_β, as given in Table II.

TABLE IV
SEQUENCES OF SIX ARRANGEMENTS OF FIG. 5

Case	Switching Sequence
(*a*)	$(6,6') - (6,1') - (6,2') - (1,2') - (2,2')$
(*b*)	$(6,6') - (1,6') - (1,1') - (1,2') - (2,2')$
(*c*)	$(6,6') - (1,6') - (2,6') - (2,1') - (2,2')$
(*d*)	$(6,6') - (6,1') - (1,1') - (1,2') - (2,2')$
(*e*)	$(6,6') - (6,1') - (1,1') - (2,1') - (2,2')$
(*f*)	$(6,6') - (1,6') - (1,1') - (2,1') - (2,2')$

TABLE V
NUMBER OF PROBABLE SEQUENCES OF S1–S8

Case	No. of Sequences
S1, S2	20
S3-S6	10
S7, S8	6

Number of cases for other sequence-groups can also be found in the similar manner and are given in Table V. It is important to mention here that all these possibilities may not arise in case of $\vec{m} \in \Delta OAB$. For example, it is possible to show that only two sequences, cases (*c*) and (*f*) of Table IV, can occur within $\square EDAB$ from the six possible sequences of S7. These two sequences are applied in $\square EDGF$ and $\square FGAB$, respectively, where the equation of FG in Fig. 4 is $m_\alpha + \frac{1}{2+\sqrt{3}} m_\beta = \frac{2}{1+\sqrt{3}}$.

III. DETERMINATION OF TECHNIQUE(S) WITH OPTIMAL CURRENT-RIPPLE PERFORMANCE

To minimize RMS ripple current over a line-cycle, this article proposes to minimize the ripple RMS current at every carrier cycle. The total RMS ripple current of all six phases over a carrier cycle can be derived after following the steps given in [4]. The expression of this RMS current, $\tilde{i}_{\text{RMS}}$, is

$$\tilde{i}^2_{\text{RMS}} \triangleq \sum_{j=a}^{c'} \tilde{i}^2_{j,\text{RMS}} = k_f^2 \left(\tilde{\lambda}^2_{\alpha\beta}(m_\alpha, m_\beta) + \gamma^2 \tilde{\lambda}^2_{z_1 z_2}(m_\alpha, m_\beta) \right) \tag{6}$$

where RMS ripple current of jth phase, $\tilde{i}_{j,\text{RMS}}$, and $\tilde{i}_{\text{RMS}}$ are perunitized with respect to base current $\frac{V_{\text{DC}} T_{sw}}{L_{\alpha\beta}}$. γ is a machine

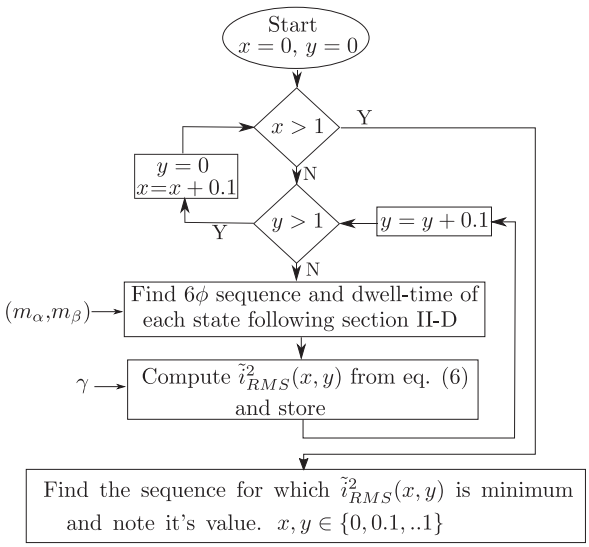

Fig. 7. Algorithm to find the optimal technique of sequence-groups S1 and S2.

parameter, which is defined as $\gamma \triangleq \frac{L_{\alpha\beta}}{L_{z_1 z_2}}$; $L_{\alpha\beta}$ and $L_{z_1 z_2}$ are the high-frequency equivalent circuit inductances in $\alpha - \beta$ and $z_1 - z_2$ planes, respectively. $\tilde{\lambda}_{\alpha\beta}$ and $\tilde{\lambda}_{z_1 z_2}$ are the ripple RMS fluxes in these two planes. In (6), the factor $k_f \triangleq \frac{T_s}{T_{\text{sw}}}$ is introduced to keep average switching frequency, $F_{\text{sw}} \triangleq \frac{1}{T_{\text{sw}}}$, same for all techniques during comparison. It can be seen that $\tilde{i}_{\text{RMS}}$ depends only on modulation technique and γ. The parameter γ is a strong function of winding pitch-factor and geometry of the slot of the machine. The full-pitched winding machine has the smallest γ value, whereas the highest value of γ occurs at $5/6$th pitch factor [15]. The full-pitched winding machine used in [4] has $\gamma = 1.58$, the machine with $5/6$th pitch factor has $\gamma = 11$. The full-pitched winding machine, used for experimental verification in this work, has $\gamma = 1.69$. Based on these aspects, the feasible range of γ is considered to be 1.5–10 in this work.

With the above formulation, the optimal technique is found numerically rather than analytically due to the complex nature of the problem. The algorithm to find the optimal technique, for a given $\vec{m} \triangleq m_\alpha + jm_\beta$ and machine parameter γ, is explained as follows.

1) *Step-1:* The optimal sequence of a particular sequence-group is identified, and the corresponding $\tilde{i}^2_{\text{RMS}}$ is recorded. A flowchart of this step is given in Fig. 7 for sequence-groups S1 and S2. Here, values of x and y are varied between 0 and 1 with the spacing of 0.1 between two consecutive values. A similar procedure can be followed to find the optimal sequence and corresponding ripple RMS currents of sequence groups S3–S6 (either x or y varies), S7, and S8 (only one sequence).
2) *Step-2:* Based on the conditions given in (5), there could be a maximum of eight optimal sequences, one coming from each sequence group, S1–S8. From these eight (or less than 8) sequences, find the sequence for which $\tilde{i}^2_{\text{RMS}}$ is minimum. For the given $\vec{m}$ and γ, this sequence is the optimal sequence out of all possible sequences, which follow the rules *R1* and *R2*.

The aforementioned algorithm is run for a range of $\vec{m} \in \Delta OAB$ and the feasible range of γ. Fig. 8 shows region-wise optimal techniques for three values of γ within ΔOAB. It is interesting to notice that only five techniques, out of so many possibilities, are optimal for most of the region of ΔOAB for $1.5 \leq \gamma \leq 10$. These are labeled as optimal linear technique-1/OLT-1–OLT-5. Table VI tabulates 6ϕ sequences, type of $\alpha - \beta$ plane vectors used, and the sequence-group and corresponding x, y values of these techniques. Please refer to these states from Fig. 2(a), where the nonzero voltage vectors are of three different lengths-large (L), medium (M), and small (S). The zero vector, (z, z'), where $z \in \{0, 7\}$, is denoted by Z. Other optimal techniques, like, S2, $x = 0.6$, $y = 0.5$ and S2, $x = 0.5$, $y = 0.4$, show optimality for very small region at $1.5 \leq \gamma \leq 2$ and are neglected for practical implementation. One should note that OLT-1 is the same as existing C 6ϕ SVPWM24-C [7]. This is the only optimal technique that exists in the literature. Although 6ϕSVM3 of [16] uses the active vectors same as OLT-2, zero vectors used by them are different, and so are their current-ripple performances.

Let's define $\psi^2_{\alpha\beta} \triangleq k_f^2 \tilde{\lambda}^2_{\alpha\beta}$ and $\psi^2_{z_1 z_2} \triangleq k_f^2 \tilde{\lambda}^2_{z_1 z_2}$. The analytical closed-from expressions of $\psi^2_{\alpha\beta}$ and $\psi^2_{z_1 z_2}$ of all of the above optimal vector-sequences are derived and these are fourth- and third-order polynomials, respectively, of two variables, m_α and m_β. The generalized analytical expressions of $\psi^2_{\alpha\beta}$ and $\psi^2_{z_1 z_2}$ is given in (7) shown at the bottom of the next page, and Table VII lists the coefficients of these polynomial expressions of five optimal techniques. Few important observations of this study are as follows.

1) Based on the set of optimal techniques, that one needs to consider for the entire ΔOAB, the feasible value of γ can fall in three following ranges.
   1) Low ($1.5 \leq \gamma \leq 3.5$), where OLT-1 to OLT-4 are used.
   2) Medium ($3.5 \leq \gamma \leq 8$), where OLT-1, OLT-2, OLT-4, and OLT-5 are used.
   3) High ($8 \leq \gamma \leq 10$), where OLT-1, OLT-2, and OLT-5 are used.
2) OLT-1 shows optimality at low voltage gain; OLT-2 for medium voltage gain; and OLT-3, OLT-4, and OLT-5 at higher voltage gain.

If the γ value for any machine is outside the above range, one can still follow the above steps to find the optimal technique(s) for that particular γ value. Even at $\gamma = 1.3$ and $\gamma = 25$, the optimality of the above five techniques is valid.

IV. Proposed Hybrid Optimal Technique

Based on the machine parameter, γ, falling in one of the three ranges, one can easily identify the optimal techniques in the entire region of a sector and thereafter, implement a optimal technique at every carrier-cycle for the given $\vec{m}$. To know the boundary between the optimal regions of ith and jth optimal techniques, one needs to equate their carrier-cycle RMS ripple current as given in (6), i.e., $(\psi^2_{\alpha\beta} + \gamma^2 \psi^2_{z_1 z_2})_i =$

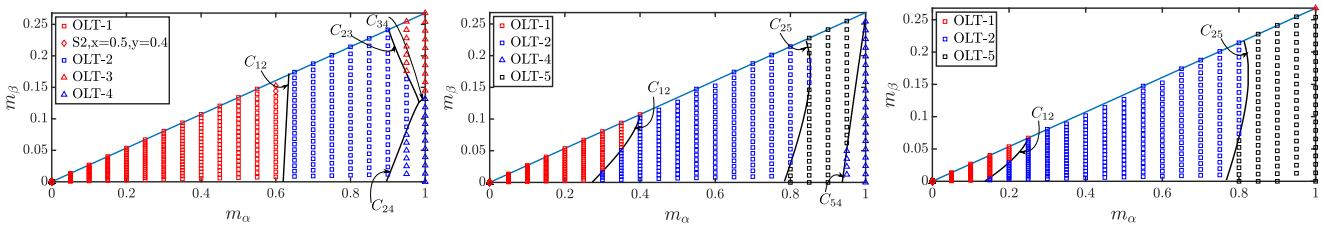

Fig. 8. Region-wise optimal techniques for different values of γ. (a) $\gamma = 2$. (b) $\gamma = 6$. (c) $\gamma = 10$.

TABLE VI
OPTIMAL FIVE LINEAR PWM TECHNIQUES OF ASPM

OLTs	Switching sequence over $\frac{T_s}{2}$	Vector type	Sequence-group, x, y
OLT-1	$(0,7') - (0,6') - (1,1') - (2,1') - (7,1') - (7,0')$	3L+2S+2Z	S2, $x = 0.5$, $y = 0.5$
OLT-2	$(0,7') - (0,6') - (1,6') - (1,1') - (2,1')$	3L+1S+1Z	S2, $x = 1$, $y = 1$
OLT-3	$(0,6') - (1,6') - (1,1') - (2,1') - (2,0')$	3L+2S	S2, $x = 1$, $y = 0$
OLT-4	$(6,6') - (1,6') - (1,1') - (2,1') - (2,0')$	4L+1S	S6, $y = 0$
OLT-5	$(6,6') - (1,6') - (1,1') - (2,1') - (2,2')$	5L	S7

TABLE VII
COEFFICIENTS OF $\psi^2_{\alpha\beta}(m_\alpha, m_\beta)$ AND $\psi^2_{z_1z_2}(m_\alpha, m_\beta)$ OF DIFFERENT TECHNIQUES (MULTIPLIED BY 1000)

Techniques		C_1	C_2	C_3	C_4	C_5	C_6	C_7	C_8	C_9	C_{10}	C_{11}	C_{12}	C_{13}	C_{14}	C_{15}
OLT-1	$\psi^2_{\alpha\beta}$	18.2	0	46.9	-36.1	49.5	-37.2	8.9	-64.6	-19.1	20.8	0	20.8	0	0	0
	$\psi^2_{z_1z_2}$	0	0	0	0	0	1.8	-8.9	15.3	5.2	0	0	0	0	0	0
OLT-2	$\psi^2_{\alpha\beta}$	32.4	16	27.8	16	32.4	-68.5	-13.9	-55.6	-54.4	37	0	37	0	0	0
	$\psi^2_{z_1z_2}$	0	0	0	0	0	0.9	-5.9	13.9	-3.6	0	0	0	0	0	0
OLT-3	$\psi^2_{\alpha\beta}$	32.4	32.1	27.8	-32.1	32.4	-103.2	-73.7	-35.8	-6.3	120.9	59.8	17.3	-59.8	-16	-10.7
	$\psi^2_{z_1z_2}$	0	0	0	0	0	35.7	37.9	-5.9	-3.6	-83.9	-59.9	19.8	59.9	16	-10.7
OLT-4	$\psi^2_{\alpha\beta}$	32.4	8	69.4	-24.1	18.5	-73.3	-40.1	-102.1	24.1	33.3	59.9	22.2	16	-27.8	-6.2
	$\psi^2_{z_1z_2}$	0	0	0	0	0	37.8	32.1	-3.7	0	-79.6	-59.9	5.5	48.1	27.8	-6.2
OLT-5	$\psi^2_{\alpha\beta}$	32.4	-8	69.4	24.1	18.5	-27.8	28.4	-80.2	-24.1	-83	-48.1	0.4	103.7	27.8	-23
	$\psi^2_{z_1z_2}$	0	0	0	0	0	13.9	11.7	2.1	0	-28.1	-16	-0.3	16	4.3	-1.7

$(\psi^2_{\alpha\beta} + \gamma^2\psi^2_{z_1z_2})_j$ and these expressions are given in (7) and Table VII as the function of m_α and m_β. The boundary between ith and jth optimal techniques, denoted by $C_{ij}, i, j \in \{1, 2, ..5\}$, is shown in Fig. 8.

This proposed hybrid optimal technique is compared in Fig. 9 with the existing LMTs of ASPM, which are discussed in Section I. For this comparison, the carrier-cycle ripple current are integrated over a line-cycle for sinusoidal excitation in $\alpha - \beta$ with $\vec{m} = \sqrt{3}M_I e^{j\omega_o t}$ and zero average voltage excitation in $z_1 - z_2$ to get the line-cycle total ripple current RMS as function of M_I. Applying inverse transformation of T on these transformed domain voltages, one can obtain the phase voltages as $\overline{v}_{ao} = M_I V_{\text{DC}} \cos\omega_o t$, $\overline{v}_{a'o'} = M_I V_{\text{DC}} \cos(\omega_o t - \frac{\pi}{6})$; $\overline{v}_{bo/b'o'}$ and $\overline{v}_{co/c'o'}$ are 120° and 240° phase-shifted with respect to $\overline{v}_{ao/a'o'}$. Here, M_I is modulation index, which is defined as the ratio of peak of the fundamental line-neutral voltage and dc-bus voltage. The line-cycle RMS of the ripple current of each phase, $\tilde{I}_{\text{RMS}}$, can be obtained from (6) as

$$\tilde{I}^2_{\text{RMS}}(M_I) = \frac{1}{6}\left(\frac{1}{2\pi}\int_0^{2\pi} \tilde{i}^2_{\text{RMS}}(M_I, \omega_o t)d(\omega_o t)\right) \quad (8)$$

which is also per-unitized with respect to base current $\frac{V_{\text{DC}}T_{\text{sw}}}{L_{\alpha\beta}}$. As $\tilde{i}_{\text{RMS}}$ denotes switching cycle RMS current combining all six phases, and total ripple RMS current seen by all six phases over a line-cycle is same, factor $\frac{1}{6}$ is introduced in (8) to obtain $\tilde{I}^2_{\text{RMS}}$ of each phase. For fair comparison, we have chosen five existing techniques, which follow rules *R1* and *R2*; these are 1) D 6ϕ SVPWM24-B2, the best technique of [6], 2) C 6ϕ SVPWM24-C, 3) Three TINV based techniques (STPWM, DZIPWM, ZS6PWM). As 6ϕSVM3 of [16] and C 6ϕ SVPWM24-C have similar performances for all γ values, 6ϕSVM3 is not considered

$$\begin{aligned}\psi^2_{\alpha\beta/z_1z_2}(m_\alpha, m_\beta) = {} & (C_1 m_\alpha^4 + C_2 m_\alpha^3 m_\beta + C_3 m_\alpha^2 m_\beta^2 + C_4 m_\alpha m_\beta^3 + C_5 m_\beta^4) \\ & + (C_6 m_\alpha^3 + C_7 m_\alpha^2 m_\beta + C_8 m_\alpha m_\beta^2 + C_9 m_\beta^3) \\ & + (C_{10} m_\alpha^2 + C_{11} m_\alpha m_\beta + C_{12} m_\beta^2) + (C_{13} m_\alpha + C_{14} m_\beta) + C_{15}. \end{aligned} \quad (7)$$

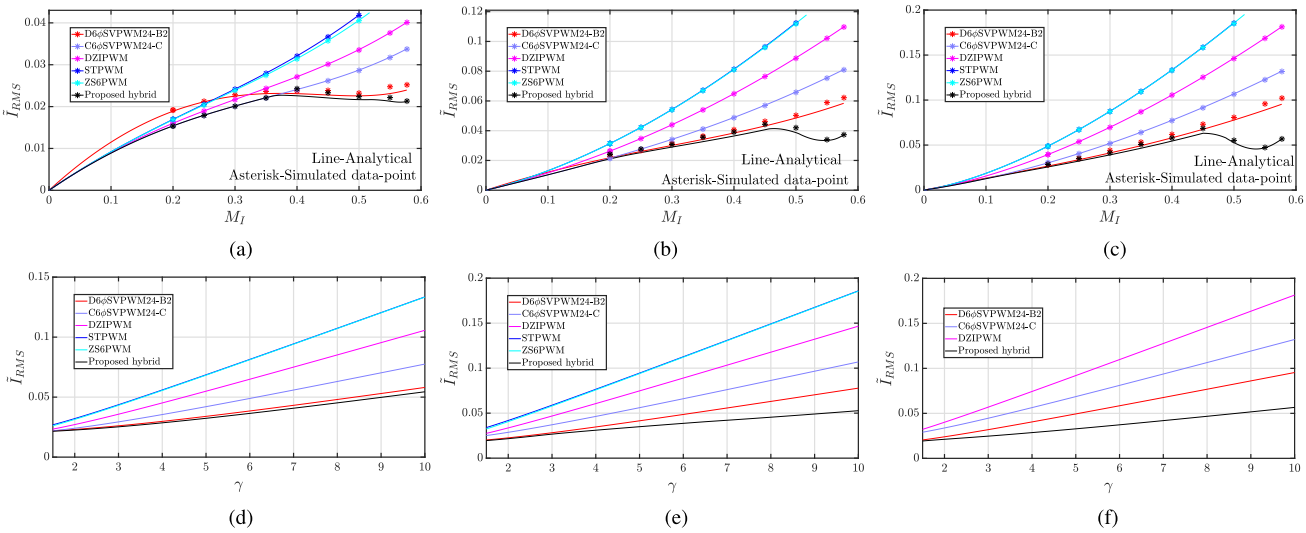

Fig. 9. Comparison of the ripple current performances of five existing techniques and the proposed hybrid technique. (a) $\tilde{I}_{\text{RMS}}$ versus M_I at $\gamma = 2$. (b) $\tilde{I}_{\text{RMS}}$ versus M_I at $\gamma = 6$. (c) $\tilde{I}_{\text{RMS}}$ versus M_I at $\gamma = 10$. (d) $\tilde{I}_{\text{RMS}}$ versus γ at $M_I = 0.4$. (e) $\tilde{I}_{\text{RMS}}$ as function of γ at $M_I = 0.5$. (f) $\tilde{I}_{\text{RMS}}$ as function of γ at $M_I = 0.577$.

TABLE VIII
k_f OF DIFFERENT TECHNIQUES

Technique	k_f	Technique	k_f
D6ϕSVPWM24-B2	$\frac{2}{3}$	C6ϕSVPWM24-C / OLT-1	1
STPWM, ZS6PWM, DZIPWM	1	OLT-2/3/4/5	$\frac{2}{3}$

separately in this comparison. As all of the 12-sector based techniques of [4] disobey rule *R1*, they are not included in this comparison. k_f values of different techniques are considered as given in Table VIII to keep the average switching frequency same. $\tilde{I}_{\text{RMS}}$ versus M_I for three fixed γ values (2, 6, and 10) of five existing techniques and the proposed hybrid technique are plotted in Fig. 9(a)–(c) up to the maximum attainable M_Is, which are 0.5 and 0.517 for STPWM and ZS6PWM, respectively, and 0.577 for other cases. The curves shown in these plots correspond to the analytical plots and the asterisk marks correspond to the simulated data-points, which will be referred later. Fig. 9(d)–(f) shows the analytical plots of $\tilde{I}_{\text{RMS}}$ as function of γ in the range of $1.5 \leq \gamma \leq 10$ for three fixed values of M_I,. viz, 0.4, 0.5, and 0.577, respectively. As the maximum M_Is attainable by STPWM and ZS6PWM are less than 0.577, these techniques are absent during comparison at $M_I = 0.577$ in Fig. 9(f).

Fig. 9 shows that $\tilde{I}_{\text{RMS}}$ of the proposed technique is the lowest among all of the techniques for the entire range of M_I and all values of γ. This proves the superiority of the proposed hybrid optimal technique over other existing techniques. As OLT-1 is the same as C 6ϕ SVPWM24-C, at low M_I, the proposed hybrid technique follows the curve of C 6ϕ SVPWM24-C. At higher values of γ and M_I, the improvement of the proposed hybrid technique compared to the existing techniques becomes more evident. At the maximum M_I, i.e., $M_I = 0.577$ and at $\gamma = 10$, $\tilde{I}_{\text{RMS}}$ of the proposed hybrid technique and the best existing technique (D 6ϕ SVPWM24-B2) are 0.0566 and 0.0954, respectively. This shows that the proposed technique reduces the ripple current RMS by 68.55 % at $M_I = 0.577$ and $\gamma = 10$ compared to the best known existing technique. This improvement results in a reduction in copper loss due to the ripple currents, and hence, the efficiency of the drive improves. The improvement in efficiency is significant in the case of medium-voltage fed high-power drives, where the base current is high due to higher V_{DC} and lower F_{sw}. Please see the Appendix for one such example.

It is discussed at the beginning of this section that one needs to evaluate $(\psi_{\alpha\beta}^2 + \gamma^2 \psi_{z_1 z_2}^2)$ of the OLTs to determine the OLT be implemented in the next carrier-cycle. This is one additional step that the proposed technique requires compared to the other existing methods. This step is calculation intensive.

To show the possible carrier-based implementation of the proposed technique, Fig. 10 shows two 180° phase-shifted triangular carriers, C_+ or C_-, which vary linearly from 0 to 1, and the comparison of duty signals with these carriers to obtain OLT-2 in sector-1. Here, d_j and S_j are the duty-ratio and the corresponding gating-signal of the top switch of jth-leg. As $S_a = S_b = S_c = 0$ and $S_{a'} = S_{b'} = S_{c'} = 1$ at the starting of the carrier cycle, d_a, d_b, and d_c are compared with C_+ and $d_{a'}$, $d_{b'}$, $d_{c'}$ are compared with C_-. Sequences of other OLTs can also be generated using C_+ and C_- in the similar manner. The gating signals of the bottom switches are obtained after complementing the gating-signals of the top switches and incorporating dead-time to it.

One should note that when a single OLT is followed, the optimal switching sequences never cause multiple switching commutations during the transition from one state to another. When the reference voltage vector, $\vec{m}$, moves from the region of one OLT to another OLT, then also it is possible to avoid multiple commutations at the point of transition if the transiting switching states accord to the Table IX.

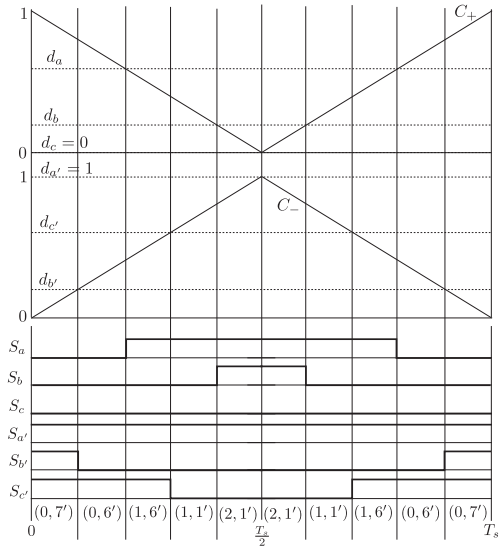

Fig. 10. Carrier-comparison based implementation of OLT-2 in sector-1 of $\alpha - \beta$ plane.

TABLE IX
TRANSITING SWITCHING STATES FOR ALL POSSIBLE TRANSITIONS OF OLTS

Transiting techniques	Transiting switching state
OLT-1 ↔ OLT-2	$(0, 7') \leftrightarrow (0, 7')$
OLT-2 ↔ OLT-3	$(0, 7') \leftrightarrow (0, 6')$ or $(2, 1') \leftrightarrow (2, 0')$
OLT-2 ↔ OLT-4	$(2, 1') \leftrightarrow (2, 0')$
OLT-3 ↔ OLT-4	$(2, 0') \leftrightarrow (2, 0')$
OLT-2 ↔ OLT-5	$(2, 1') \leftrightarrow (2, 2')$
OLT-4 ↔ OLT-5	$(6, 6') \leftrightarrow (6, 6')$

(a) (b)

Fig. 11. Experimental set-up. (a) Six-phase inverter and controller. (b) ASPM coupled with dc generator.

TABLE X
EQUIVALENT CIRCUIT PARAMETERS OF 6ϕ IM

Per phase stator and rotor resistances (50 Hz)	0.675 Ω
Per phase magnetizing inductance (50 Hz)	0.186 H
Per phase stator and rotor leakage inductances (50 Hz)	3.75 mH
High-frequency $\alpha - \beta$ plane inductance, $L_{\alpha\beta}$	4.2 mH
High-frequency $z_1 - z_2$ plane inductance, $L_{z_1 z_2}$	2.5 mH
Ratio of inductances in $\alpha - \beta$ and $z_1 - z_2$, γ	1.69

V. SIMULATION AND EXPERIMENTAL VALIDATION

Fig. 11(b) shows a 2-pole 5 kW asymmetrical 6ϕ squirrel-cage induction machine, coupled with a dc generator for loading purposes, which is used for experimental validation. The equivalent circuit parameters of this machine are given in Table X. Due to the skin effect of the rotor bars in squirrel-cage motor, $L_{\alpha\beta}$ and $L_{z_1 z_2}$ seen by the switching-frequency ripple current are different from the equivalent 50 Hz values ($L_{\alpha\beta}$=7.42 mH, $L_{z_1 z_2}$=3.75 mH at 50 Hz) [17]. The switching frequency inductance values in $\alpha - \beta$ and $z_1 - z_2$ planes can be determined from the piecewise constant voltage applied by the PWM technique and the corresponding slope in the current waveforms. These high-frequency inductance values are indicated in Table X. γ of this full-pitched winding machine is 1.69. SKM75GB123D IGBT-based 6ϕ inverter along with Zynq-7010 based controller card is shown in Fig. 11(a). Simulation is done using Simscape's specialized power system toolbox of MATLAB-Simulink. In the Simulink model, ideal switches are used in the 6ϕ inverter, and the differential equations of the dynamic model of ASPM, as given in [3], are implemented in Laplace's transformed domain. Bogacki Shampine solver with a fixed step-size of 1 μs is used in the simulation. The simulation scheme is shown in Fig. 12. The load–torque–calculator block in Fig. 12 estimates the load torque, which is equivalent to loading a dc generator with its output dc voltage connected across a fixed value resistive load (45 Ω). When the inverter output frequency is 50 Hz, the output voltage of the dc generator is 400 V. During the experiment, 800 ns dead-time is incorporated between the two complementary switches of one leg of 6ϕ inverter. Tektronix P5200 A differential voltage probes, TCP0030 A current probes, MDO3104, and MSO2024B oscilloscope are used to capture the experimental waveforms.

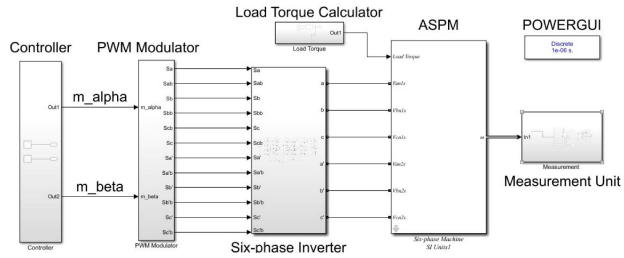

Fig. 12. MATLAB scheme for the simulation.

Experiments and simulations are performed at nine values of M_I between 0.2 and 0.577, viz $M_I \in \{0.2, 0.25, 0.3, 0.35, 0.4, 0.45, 0.5, 0.55, 0.577\}$, with following operating conditions: V_{DC}= 300 V; F_{sw} =8.33 kHz. For constant V/f operation, M_I is changed along with output frequency, f_o, which results into 50 Hz operation at maximum M_I (0.577). As the machine used in the experiment has $\gamma = 1.69$ (belongs to low range), the hybrid optimal technique involves OLT-1 to OLT-4, as discussed in Section III. k_f of OLT-1 is 1 and k_f of other OLTs is 2/3. Therefore, based on the position of $\vec{m}$ in one of the four OLTs, the carrier frequency is changed between 8.33 kHz and 12.5 (8.33 ×3/2) kHz. Fig. 13(a) and (d) shows the experimental and simulated four sinusoidal line currents, i_a, $i_{a'}$, i_b, and $i_{b'}$; Fig. 13(b) and (e) shows the corresponding two line-line voltages, v_{ab} and $v_{a'b'}$; and Fig. 13(c) and (f) shows three-phase line-neutral voltages, v_{ao}, v_{bo}, v_{co} of the proposed optimal technique at $M_I = 0.577$, $f_o = 50$ Hz, and output power of 3.55 kW. The fundamental operation of ASPM in linear region can be verified from 30° phase-shifted pairs, $\{v_{ab}, v_{a'b'}\}$, $\{i_a, i_{a'}\}$, $\{i_b, i_{b'}\}$ and 120° phase-shifted $\{i_a, i_b\}$, $\{i_{a'}, i_{b'}\}$, and $\{v_{ao}, v_{bo}, v_{co}\}$. The close observation to the unexpected opposite polarity voltage

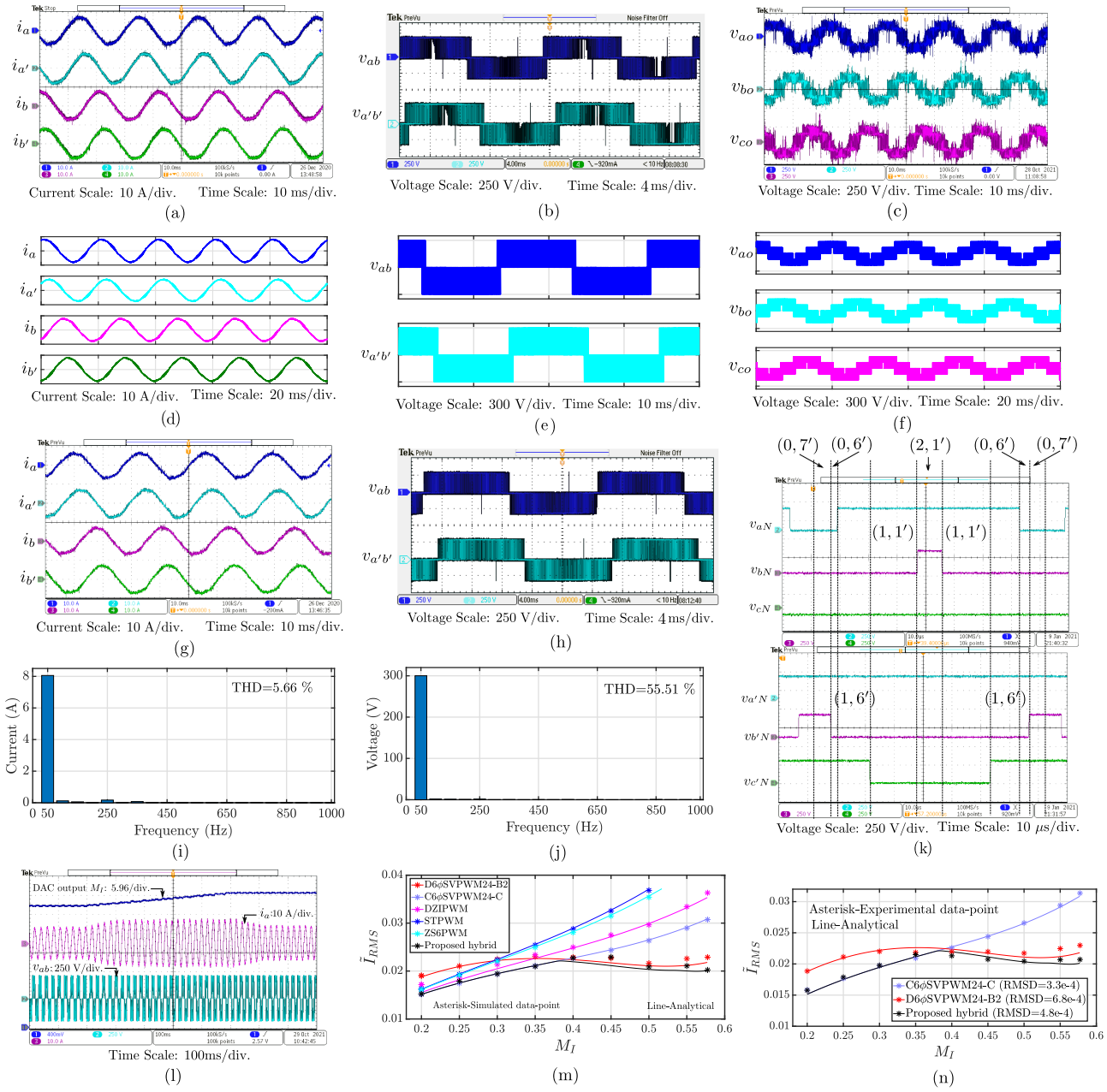

Fig. 13. Experimental and simulation waveforms of proposed technique and ripple-current comparison with existing techniques. (a) Experimental i_a, $i_{a'}$, i_b, $i_{b'}$ at $M_I = 0.577$. (b) Experimental v_{ab}, $v_{a'b'}$ at $M_I = 0.577$. (c) Experimental v_{ao}, v_{bo}, v_{co} at $M_I = 0.577$. (d) Simulated i_a, $i_{a'}$, i_b, $i_{b'}$ at $M_I = 0.577$. (e) Simulated v_{ab}, $v_{a'b'}$ at $M_I = 0.577$. (f) Simulated v_{ao}, v_{bo}, v_{co} at $M_I = 0.577$. (g) Experimental i_a, $i_{a'}$, i_b, $i_{b'}$ at $M_I = 0.5$. (h) Experimental v_{ab}, $v_{a'b'}$ at $M_I = 0.5$. (i) Spectrum of experimental i_a at $M_I = 0.577$. (j) Spectrum of experimental v_{ab} at $M_I = 0.577$. (k) Experimentally obtained sequence when OLT-2 is applied in sector-1. (l) Experimental result of speed variation. (m) Simulated $\tilde{I}_{\text{RMS}}$ vs. M_I at $\gamma = 1.69$. (n) Experimental $\tilde{I}_{\text{RMS}}$ vs. M_I at $\gamma = 1.69$.

spikes, appearing once in every half-cycle of experimental v_{ab}, $v_{a'b'}$ waveforms, reveals that the width of this voltage pulse is same as dead-time used in the implementation, i.e., 1 μs. This occurs when two legs undergo dead-time period simultaneously, and therefore, the voltage between these two legs is defined by the diodes in conduction (or the current directions in those two legs), which may be of opposite polarity. Fig. 13(i) and (j) shows the frequency spectrum of experimentally obtained phase current, i_a, and line–line voltage, v_{ab}, respectively, upto 20th order harmonics (1 kHz) for $M_I = 0.577$. The peak of the fundamental components of these current and voltage is 8.06 A and 300.11 V. Fig. 13(g) and (h) shows the four phase currents and two line–line voltage waveforms at $M_I = 0.5$, $f_o = 43.33$ Hz, and output power of 2.82 kW. The peaks of the fundamental components of these are 7.2 A and 260.73 V, respectively. Although no significant low-frequency harmonic is present in v_{ab} spectrum, small amount of fifth harmonic [0.17 A in Fig. 13(i)] is present in phase current, which arises due to

machine or converter asymmetry or dead-time of the inverter and is unavoidable in case of ASPM running in open-loop [18]. Therefore, the harmonic distortions present in the voltages and currents are mainly switching-frequency ripple and the total harmonic distortions (THDs) of the experimental i_a and v_{ab} are 5.66% and 55.51%, respectively. Fig. 13(k) shows the six pole voltages, v_{xN}, when $\vec{m} = \sqrt{3} \times 0.4e^{j7.5^\circ}$ lies in sector-1 and the proposed hybrid technique applies OLT-2. Here, $x \in \{a, b, c, a,' b,' c'\}$ and N is dc-bus negative terminal. The switching sequence applied by 6ϕ inverter can be derived from this diagram, which is $(0, 7') - (0, 6') - (1, 6') - (1, 1') - (2, 1') - (1, 1') - (1, 6') - (0, 6') - (0, 7')$. This sequence matches with the sequence given in Table VI. Fig. 13(l) shows M_I (brought out from the controller through DAC), i_a, and v_{ab} waveforms under the variable speed operation of ASPM, where the (M_I, f_o) pair is changed from (0.52, 45 Hz) to (0.577, 50 Hz) in 0.5 s keeping V/f constant. The phase current i_a increases during transient and settled down again in steady-state value.

The analytical performance comparison of the proposed technique with existing techniques, as discussed in Section IV, is first validated through simulation at $\gamma = 2, 6, 10$. These simulated data-points are shown in Fig. 9(a)–(c), respectively, by the asterisk marks. The carrier frequency, $F_s = \frac{F_{sw}}{k_f}$, is varied from one technique to another based on k_f values, as given in Table VIII. As the simulated data points are closely following the analytical plots, this study also reaches the same conclusion about the optimality of the proposed technique as discussed in Section IV. Fig. 13(m) shows both the analytical and simulated performance comparison at $\gamma = 1.69$ from where it can be seen that D 6ϕ SVPWM24-B2 and C 6ϕ SVPWM24-C are two best performing existing techniques at this γ value. Therefore, these two techniques are chosen along with the proposed PWM strategy for experimental validation of performance comparison. Fig. 13(n) shows this ripple-current comparison. At lower M_I, C 6ϕ SVPWM24-C and proposed technique performs in the similar manner, which is better than D 6ϕ SVPWM24-B2. As M_I increases, the performance of D 6ϕ SVPWM24-B2 becomes better than C 6ϕ SVPWM24-C, and the proposed hybrid optimal technique is superior compared to both of these techniques. To calculate $\tilde{I}_{\text{RMS}}$ of the experimental and simulated waveforms, sampled data-point at a regular interval of 1 μs of a phase current is stored and then processed in the MATLAB script file. The experimental phase current contains 1) fundamental component; 2) few lower-order harmonics due to converter or machine asymmetry or dead-time, as explained before; 3) ripple components at switching frequency and its multiples; and 4) high-frequency transient noise occurring due to transition in six-phase inverter legs. The magnitudes of low-frequency components are negligible after 20th harmonics (maximum 1 kHz). It has been verified through simulation, where the high-frequency switching transient noise is absent in current waveforms that the amplitudes beyond 100 kHz are negligible. Therefore, during evaluation of $\tilde{I}_{\text{RMS}}$ of the experimental and simulated current waveforms, RMS currents due to 1 to 100 kHz are considered ($F_{\text{sw}} =$ 8.33 kHz) so that only the ripple components are accounted. The maximum error between the experimental and the analytical values of Fig. 13(n) is 6% and the root-mean-square deviation (RMSD) of the experimental results of C 6ϕ SVPWM24-C, D 6ϕ SVPWM24-B2 and the proposed strategy are 3.3e-4, 6.8e-4, and 4.8e-4, respectively.

VI. Conclusion

This article accounts for an exhaustive set of LMTs of the ASPM, which avoids a major disadvantage present in a few existing LMTs–turning ON and turning OFFa device more than one time within a carrier period. It increases the instantaneous switching frequency of the device for a given average switching frequency. This article first identifies the sequences per three-phase (3ϕ) inverter basis, where the above limitation was overcome. After that, combining the sequences of two 3ϕ inverters, this article forms eight sequence-groups. The number of possible techniques in six sequence-groups was infinite because the zero-vector dwell-times of two 3ϕ inverters can be distributed between the redundant zero states in infinite possible ways. This distribution impacts the current ripple of LMTs. After comparing the current-ripple performances of the techniques of all eight sequence-groups, this article identifies five techniques, which show the optimality within the entire linear region for the whole feasible range of the machine parameter, γ. Only one of these five techniques exists in the literature. After that, an optimal hybrid strategy was proposed, which applies the best of these five techniques in each carrier cycle depending upon the position of the reference voltage vector. For any given γ within the feasible range, the proposed hybrid optimal strategy shows the best ripple current performance in the entire range of modulation indices compared with the existing best-performing techniques, which do not have the disadvantage mentioned above. The proposed strategy shows 68.55% improvement in the ripple performance compared to the existing best-known PWM technique at maximum modulation index for $\gamma = 10$. The implementation of this PWM technique involves evaluation of current-ripples of a few optimal methods. This step was calculation-intensive. Simplification of this step and after that finding carrier-based implementation is the possible future work. The theoretical analysis was verified through simulation and experiment on an ASPM with $\gamma = 1.69$ up to 3.5 kW power level.

Appendix
Example of Efficiency Improvement in Medium-Voltage High-Power Machine

Let us consider a 150 h.p. (110 kW), 2 kV, 3ϕ, 50 Hz, 600 RPM, slip-ring induction motor, B.S.S. 168-1936 machine, whose design is given in [19]. The required V_{DC} to drive this machine in ASPM configuration is 1.5 kV. The machine parameters in 3ϕ configuration are derived in [19] from which the approximate equivalent parameters in 6ϕ configuration are deducted. The short-circuit resistance, $L_{\alpha\beta}$ are 0.675 Ω and 4.23 mH; let the γ of the machine is 10. Let, F_{sw} of this high-power drive is limited to 1.5 kHz. Therefore, the base current, $\frac{V_{\text{DC}} T_{\text{sw}}}{L_{\alpha\beta}}$, is 236.41 A. The expected performance for $\gamma = 10$ is given in Fig. 9(c), from where the copper losses occur at $M_I = 0.577$

due to the proposed hybrid technique and the existing best technique (D 6ϕ SVPWM24-B2) are estimated. These values are 565.8 W and 2264 W, respectively. Therefore, the proposed technique improves the efficiency by 1.54% compared to the best state-of-the-art technique.

REFERENCES

[1] F. Barrero and M. J. Duran, "Recent advances in the design, modeling, and control of multiphase machines—part I," *IEEE Trans. Ind. Electron.*, vol. 63, no. 1, pp. 449–458, Jan. 2016.

[2] A. S. Abdel-Khalik, A. M. Massoud, and S. Ahmed, "Effect of DC-link voltage limitation on postfault steady-state performance of asymmetrical six-phase induction machines," *IEEE Trans. Ind. Electron.*, vol. 65, no. 9, pp. 6890–6900, Sep. 2018.

[3] Y. Zhao and T. A. Lipo, "Space vector PWM control of dual three-phase induction machine using vector space decomposition," *IEEE Trans. Ind. Appl.*, vol. 31, no. 5, pp. 1100–1109, Sep./Oct. 1995.

[4] D. Hadiouche, L. Baghli, and A. Rezzoug, "Space-vector PWM techniques for dual three-phase AC machine: Analysis, performance evaluation, and DSP implementation," *IEEE Trans. Ind. Appl.*, vol. 42, no. 4, pp. 1112–1122, Jul./Aug. 2006.

[5] P. R. Rakesh and G. Narayanan, "Analysis of sine-triangle and zero-sequence injection modulation schemes for split-phase induction motor drive," *IET Power Electron.*, vol. 9, no. 2, pp. 344–355, 2016.

[6] K. Marouani, L. Baghli, D. Hadiouche, A. Kheloui, and A. Rezzoug, "A new PWM strategy based on a 24-sector vector space decomposition for a six-phase VSI-fed dual stator induction motor," *IEEE Trans. Ind. Electron.*, vol. 55, no. 5, pp. 1910–1920, May 2008.

[7] C. Wang, K. Wang, and X. You, "Research on synchronized SVPWM strategies under low switching frequency for six-phase VSI-fed asymmetrical dual stator induction machine," *IEEE Trans. Ind. Electron.*, vol. 63, no. 11, pp. 6767–6776, Nov. 2016.

[8] A. M. Hava, R. J. Kerkman, and T. A. Lipo, "Simple analytical and graphical methods for carrier-based PWM-VSI drives," *IEEE Trans. Power Electron.*, vol. 14, no. 1, pp. 49–61, Jan. 1999.

[9] A. Bakhshai, G. Joos, and H. Jin, "Space vector PWM control of a split-phase induction machine using the vector classification technique," in *Proc. 13th Annu. Appl. Power Electron. Conf. Expo.*, 1998, pp. 802–808.

[10] R. Bojoi, A. Tenconi, F. Profumo, G. Griva, and D. Martinello, "Complete analysis and comparative study of digital modulation techniques for dual three-phase AC motor drives," in *Proc. IEEE 33rd Annu. Conf. Power Electron. Specialists*, 2002, pp. 851–857.

[11] S. Paul and K. Basu, "A three-phase inverter based overmodulation strategy of asymmetrical six-phase induction machine," *IEEE Trans. Power Electron.*, vol. 36, no. 5, pp. 5802–5817, May 2021.

[12] J. Prieto, E. Levi, F. Barrero, and S. Toral, "Output current ripple analysis for asymmetrical six-phase drives using double zero-sequence injection PWM," in *Proc. IEEE 37th Annu. Conf. Ind. Electron. Soc.*, 2011, pp. 3692–3697.

[13] V. Blasko, "Analysis of a hybrid PWM based on modified space-vector and triangle-comparison methods," *IEEE Trans. Ind. Appl.*, vol. 33, no. 3, pp. 756–764, May/Jun. 1997.

[14] D. G. Holmes, "The significance of zero space vector placement for carrier-based PWM schemes," *IEEE Trans. Ind. Appl.*, vol. 32, no. 5, pp. 1122–1129, Sep./Oct. 1996.

[15] D. Hadiouche, H. Razik, and A. Rezzoug, "On the modeling and design of dual-stator windings to minimize circulating harmonic currents for VSI fed AC machines," *IEEE Trans. Ind. Appl.*, vol. 40, no. 2, pp. 506–515, Mar./Apr. 2004.

[16] S. M. Suhel and R. Maurya, "Realization of 24-sector svpwm with new switching pattern for six-phase induction motor drive," *IEEE Trans. Power Electron.*, vol. 34, no. 6, pp. 5079–5092, Jun. 2019.

[17] M. Srndovic, R. Fišer, and G. Grandi, "Analysis of equivalent inductance of three-phase induction motors in the switching frequency range," *Electronics*, vol. 8, no. 2, 2019, Art. no. 120, doi: 10.3390/electronics8020120.

[18] H. S. Che, E. Levi, M. Jones, W.-P. Hew, and N. A. Rahim, "Current control methods for an asymmetrical six-phase induction motor drive," *IEEE Trans. Power Electron.*, vol. 29, no. 1, pp. 407–417, Jan. 2014.

[19] M. Say, *The Performance and Design of Alternating Current Machines*, 2nd ed. London, U.K.: Sir Isaac Pitman, 1957.

Sayan Paul received the B.Tech. degree from the National Institute of Technology, Durgapur, India, in 2014, the M.Sc. (Engg.) degree from Indian Institute of Science, Bangalore, India, in 2018, both in electrical engineering. He is currently working toward the Ph.D. degree in electrical engineering at Indian Institute of Science, Bangalore, India.

His research interests include PWM techniques, modeling and control of multiphase drives, multilevel converters.

Kaushik Basu (Senior Member, IEEE) received the B.E. degree in electrical engineering from the Bengal Engineering and Science University, Shibpore, India, in 2003, the M.S. degree in electrical engineering from the Indian Institute of Science, Bangalore, India, in 2005, and the Ph.D. degree in electrical engineering from the University of Minnesota, Minneapolis, MN, USA, in 2012.

He was a Design Engineer with Cold Watt India, in 2006, and an Electronics and Control Engineer with Dynapower Corporation, USA from 2013 to 2015. He is currently an Assistant Professor with the Department of Electrical Engineering, Indian Institute of Science. He has been an author and coauthor of several technical papers published in peer reviewed journals and conferences. His research interests include various aspects of the general area of power electronics.

Dr. Basu is the founding chair of both *IEEE PELS* and *IES Bangalore Chapter*.